Evolution of Dislocation Patterns in a Tricrystal Model Subjected to Cyclic Loading

Tetsuya Ohashi[1] and Ryouji Kondou[2]

[1]Kitami Institute of Technology, Koencho 165, Kitami, 090-8507, Japan
tel./fax. 81-0157-26-9227, email ohashi@newton.mech.kitami-it.ac.jp
[2]University of the Ryukyus, 1 Senbaru, Nishihara, Nakagami, Okinawa 903-0213, Japan
tel./fax. 81-0980-895-8610, email kondou@teada.tec.u-ryukyu.ac.jp

Abstract

When polycrystalline aggregate is deformed beyond elastic range, dislocations pile up at grain boundaries and make some patterned structures within grains. If the external load is reversed, most dislocations at grain boundaries and in the patterned structure are supposed to disappear or change their arrangements, but details are not yet known well. In this study, we examine such changes in dislocation structures by a crystal plasticity analysis. Models for the polycrystalline aggregates consist of three grains and the generation and degeneration of the geometrically necessary dislocations during cyclic loading are examined in detail. The results show that there are some groups of dislocations that do not dissipate but evolve upon reverse loading.

1. Introduction

When a mechanical load is repeatedly applied to metal polycrystals, fatigue deformation is induced even if the applied load is not large enough to cause macroscopic yielding of the material, and this leads to changes of macroscopic mechanical properties and to a fracture [1]. Some typical patterns of dislocations are known to develop in the microstructure of the material during the fatigue process. Changes of macroscopic mechanical properties and formation of fatigue cracks during the cyclic deformation have close relation with the formation of dislocation patterns which develop under a mechanical field taking place in the polycrystal microstructure, while our understandings on the mechanical field is not enough to describe the dislocation process in detail.

Patterned structure or dislocation walls act as a barrier for the movement of dislocations between the walls leading to a formation of internal stress field [2] and as a consequence, the whole system respond to external load as a two-phase materials [3]. Saturated pattern of dislocations after cyclic deformation with strain amplitude between 10^{-5} to 10^{-2} were experimentally examined and the pattern was shown to depend on the crystal orientation [4]. Dislocation pattern in grains with crystal orientation far from edges and vertices of stereo triangle was the bundle type.

Theoretical studies for the dislocation patterning have been made extensively [3,5,6], where dislocation pattern formation was modeled as a stability problem of homogeneously distributed dislocations without long range internal stress field. Idea of "non-local strain hardening" [5,6] introduced a new step for the theoretical modeling of non-uniformly distributed, or patterned dislocations within grains. Studies on the dislocation patterning in more detailed scales were made numerically [7] where interaction intensity of dislocations and frequency of cross slip were shown to play important roles in the development of inhomogeneous distribution of dislocations.

Effects of grain boundaries on the dislocation storage and patterning after cyclic deformation were studied experimentally [8] however, effect of constraints originating from neighboring crystal grains was observed to be complex and details were left unknown [9]. Some difficulties in understanding the mechanical field in polycrystal microstructure stem from the three dimensional structure of grain boundary networks [10]. Intersection of three grain boundary planes makes up a triple line of grain boundaries, and a quadruple point of grain boundary planes is formed where four triple lines meet. Accordingly, the three dimensional structure of a polycrystal consists of a three dimensional network of grain boundary triple lines connected at grain boundary quadruple points. At a grain boundary plane, two different kinds of mechanical effects take place due to the difference of crystal orientation of two grains; one originating from the elastic anisotropy and the other from the discontinuity of slip deformation.

At grain boundary triple junctions or at quadruple points, effects originating from interactions between two crystal grains and other additional effects are combined.

There have been a lot of studies on the deformation of bicrystals where only two crystal grains make up a specimen. Hook and Hirth [11,12] and Hirth [13] made in-depth studies about the effect of elastic anisotropy on the non-uniform multiple slip in the vicinity of a grain boundary plane, while Hauser and Chalmers [14] attempted to describe the effects of slip discontinuity at grain boundary plane. On the other hand, not many studies were made on the deformation and dislocation accumulation near grain boundary triple junctions. When some constraint is introduced at a free surface of a bicrystal where the grain boundary plane intersects, deformation near the intersecting line is analogous to that near a grain boundary triple junction because the constraint condition at the free surface mimic the constraint exerted from the third crystal grain. Deformation near this "pseudo" triple line in a bicrystal with controlled orientation relationship and subjected to monotonic load was numerically analyzed by Kondou and Ohashi [15], and they examined evolution of density distribution of dislocations. Recently, Mayama *et al*. [16] made a detailed study on the evolution of dislocation distribution in a similar bicrystal model subjected to cyclic load. They found that some strip shaped regions of high density distribution of geometrically necessary dislocations (abbreviated as GN dislocations or GNDs, hereafter) evolved from the pseudo-triple lines into grain interiors and dislocations on some secondary slip systems were observed to superimpose to those on the primary one. They found that spatial structures of dislocations were stabilized inside the grains due to this interaction between the primary and secondary slip systems.

Some studies were made also on tricrystals where crystal orientations of three grains were chosen so as that mutual constraints between any combinations of two crystal grains did not occur when the third grain was omitted, while their deformations were mutually constrained once the three grains were connected to each other [17–19]. High-density regions of GN dislocations were found to evolve from the grain boundary triple junction into grain interiors. In this paper, we employ a similar specimen of a tricrystal and examine the deformation and dislocation accumulation under tensile deformation, followed by unloading and compression down to zero nominal strain and second tensile loading. Evolution of high-density regions of GN dislocations and activity of secondary slip systems are studied and discussed.

2. Basic equations

A three-dimensional crystal plasticity finite element analysis code is employed [20–22]. Condition for the onset of plastic slip deformation of a slip system n is given by the Schmid law

as,

$$\theta^{(n)} = P_{ij}^{(n)} \sigma_{ij}, \tag{1}$$

where $\theta^{(n)}$ and σ_{ij} denote the critical resolved shear stress (abbreviated as CRSS, hereafter) on the slip system *n* and the stress tensor, respectively. $P_{ij}^{(n)}$ is the Schmid tensor of slip system *n* defined by

$$P_{ij}^{(n)} = \frac{1}{2}\left(v_i^{(n)} b_j^{(n)} + v_j^{(n)} b_i^{(n)} \right), \tag{2}$$

where $v_i^{(n)}$ and $b_i^{(n)}$ are the slip plane normal and the slip direction, respectively. Increment of plastic strain tensor due to slip increments is given by

$$\dot{\varepsilon}_{ij}^{p} = \sum_n P_{ij}^{(n)} \dot{\gamma}^{(n)}, \tag{3}$$

where $\dot{\gamma}^{(n)}$ denotes the increment of plastic shear strain on slip system *n*. Increment of the CRSS on the slip system *n* is given as follows:

$$\dot{\theta}^{(n)} = \sum_m h^{(nm)} \dot{\gamma}^{(m)}, \tag{4}$$

where $h^{(nm)}$ denotes the strain hardening parameter.

Assuming that the deformation is small and rotation of the crystal orientation is neglected, the constitutive equation for slip deformation is given by [23]

$$\dot{\varepsilon}_{ij} = \left[S_{ijkl}^{e} + \sum_n \sum_m \left\{ h^{(nm)} \right\}^{-1} P_{ij}^{(n)} P_{kl}^{(m)} \right] \dot{\sigma}_{kl}, \tag{5}$$

where S_{ijkl}^{e} denotes the elastic compliance, and the summation is made over the active slip systems.

The following Taylor type model [20] of the critical resolved shear stress is used,

$$\theta^{(n)} = \theta_0 + \sum_m \Omega^{(nm)} a \mu \tilde{b} \sqrt{\rho_S^{(m)}}, \tag{6}$$

where θ_0, a, μ, $\tilde{b}$ and $\rho_S^{(m)}$ denote the lattice friction term, a numerical factor of the order of 0.1, the elastic shear modulus, the magnitude of the Burgers vector and the density of the statistically stored dislocations (abbreviated as SSDs, hereafter) that accumulates on slip system *m*, respectively. We employ θ_0 =0, a=0.1 and μ=40GPa. Introduction of the effects of GNDs

in the Taylor type model of CRSS is possible [24] however, it is still controversial [25][26]. Experimental results indicate that GNDs on self- and co-planar slip systems do not contribute to strain hardening while GNDs of forest type contribute [26]. In this study, only the SSDs are introduced in the model of CRSS and the effect of GNDs are introduced in the model of dislocation mean free path, as shown in the following, where SSDs and GNDs of forest type obstruct movement of dislocations and they contribute to strain hardening in indirect manner.

The initial value for SSD density is set to be 10^9 m^{-2} for all the slip system. The interaction of slip systems n and m is controlled by the interaction matrix $\Omega^{(nm)}$ in Eq. (6) [20][22]. In this study, $\Omega^{(nn)}=1$ for the diagonal components and $\Omega^{(nm)}\cong 1$ for the off-diagonal components are used to represent a nearly isotropic hardening characteristic for every slip system.

The increment in the SSD density on slip system n is evaluated by

$$\dot{\rho}_S^{(n)}=\frac{c\dot{\gamma}^{(n)}}{\tilde{b}L^{(n)}}, \tag{7}$$

where a physical picture of dislocation accumulation is drawn in terms of Orowan equation, average life time of moving dislocations and their velocity [20] with c a numerical coefficient on the order of 1. If we take another approach [27] for the accumulation of SSDs where dislocation loops are emitted and accumulate in rectangular shape, we obtain the same result as Eq. (7) and c is a function of the aspect ratio of the rectangles. If the accumulated loops are square, we obtain c=2. In this study, we use c=1 for simplicity. When the mean free path is a constant, the dislocation density will increase linearly with the shear strain and this will lead to a parabolic strain hardening. While if the mean free path is a function of some internal state variables, then the strain hardening will reflect the internal state.

The following model [28] gives the mean free path $L^{(n)}$ of dislocations on slip system n,

$$L^{(n)}=\frac{c^*}{\sqrt{\sum_m \omega^{(nm)}\left(\rho_S^{(m)}+\left\|\rho_G^{(m)}\right\|\right)}}, \tag{8}$$

where c^* is a material constant of the order of 10-100 [29,30] and we assume c^*=15 in this study. Parameter $\omega^{(nm)}$ defines the contribution of dislocations on slip system m to the mean free path of dislocations moving on the slip system n. We assume $\omega^{(nm)}=0$ when slip systems n and m are identical or co-planar. Otherwise, components of $\omega^{(nm)}$ are equal to 1. $\left\|\rho_G^{(m)}\right\|$ denotes density norm of GNDs on slip system m. With this condition, SSDs and GNDs on self- and co-planar slip systems do not contribute to the mean free path while forest dislocations will shorten the mean free path of moving dislocations and this will lead to a significant strain hardening. When the initial value of $\rho_S^{(m)}$ is equal to 10^9 m^{-2} for all the slip system, the initial

value of the mean free path evaluated by Eq. (8) with the above mentioned condition for $\omega^{(nm)}$ is about 158 μm. Change of the mean free path with deformation is shown in the section 4. Figure 1 shows calculated stress strain curves of single crystals deformed by tensile load in single and double slip orientation. Here, the single crystal specimens are assumed to be perfectly uniform and thus, deformations are uniform and only SSDs accumulate in the specimen. When the crystal is at the orientation S, the stress strain relation shows a parabolic curve as a result of a constant value of dislocation mean free path, while the strain hardening ratio for the double slip orientation D is much higher than that of single slip orientation and almost straight. The latter is caused by interaction of slip systems where dislocations act as forest ones to each other and thus their mean free paths decrease rapidly.

Density norm of GN dislocations on slip system *m* denoted by $\left\|\rho_G^{(m)}\right\|$ is defined as

$$\left\|\rho_G^{(m)}\right\| = \sqrt{\left(\rho_{G,edge}^{(m)}\right)^2 + \left(\rho_{G,screw}^{(m)}\right)^2}\,, \tag{9}$$

where the edge and screw components are obtained from spatial gradients of plastic shear strain on the slip system [21] :

$$\rho_{G,edge}^{(m)} = -\frac{1}{\tilde{b}}\frac{\partial \gamma^{(m)}}{\partial \xi}\,, \qquad \rho_{G,screw}^{(m)} = \frac{1}{\tilde{b}}\frac{\partial \gamma^{(m)}}{\partial \zeta}\,. \tag{10}$$

Here, ξ and ζ denote directions parallel and perpendicular to the slip plane, respectively. The strain hardening parameter $h^{(nm)}$ is obtained from Eqs. (4), (6), (7) and (8) as

$$\begin{aligned} h^{(nm)} &= \frac{a\mu c\Omega^{(nm)}}{2L^{(m)}\sqrt{\rho_S^{(m)}}} \\ &= \frac{a\mu c\Omega^{(nm)}}{2c^*}\sqrt{\frac{\sum_k \omega^{(mk)}\left(\rho_S^{(k)} + \left\|\rho_G^{(k)}\right\|\right)}{\rho_S^{(m)}}}\,. \end{aligned} \tag{11}$$

Recently, numerically and experimentally obtained distributions of GNDs near a grain boundary plane were compared [31]. A high density strip of GNDs was numerically observed to develop from an edge of grain boundary plane in bicrystal specimen while, polychromatic X-ray diffraction analyses detected distribution of GNDs in a narrow band region which was situated close to the grain boundary edge showing that numerical data show a good agreement with experimentally observed ones.

3. Tricrystal model

Elastic compliance, magnitude of Burgers' vector and Euler angles used in this study are

shown in Table 1. The elastic compliance data are chosen to obtain elastic isotropy and the grain boundary constraint due to elastic incompatibility [11–13] will not take place.

Fig. 2(a) shows the tricrystal model employed in this study. Dimensions of crystal grains are 100×200×10 μm and the entire specimen is 200×300×10 μm. In addition to the model shown in Fig. 2(a), a modified model of tricrystal specimen is also employed where the dimension of the grains-1 and 2 remain the same, while the dimension of the grain-3 is extended to 200×200×10 μm. A brief comparison of analysis results obtained for these two models is made in section 4, while most discussion is placed on the results obtained with the model shown in Fig. 2(a), unless otherwise stated.

Crystal lattice of the three grains are supposed to be face centered cubic type and plastic slip deformation takes place on twelve combinations of $\{111\}<110>$ slip systems. Crystal orientations of grains are given by the following equation,

$$\begin{pmatrix} [100] \\ [010] \\ [001] \end{pmatrix} = \begin{pmatrix} -\sin\theta\cos\phi & \cos\theta & \sin\theta\sin\phi \\ \cos\kappa\sin\phi+\cos\theta\sin\kappa\cos\phi & \sin\theta\sin\kappa & \cos\kappa\cos\phi-\cos\theta\sin\kappa\sin\phi \\ -\sin\kappa\sin\phi+\cos\theta\cos\kappa\cos\phi & \sin\theta\cos\kappa & -\sin\kappa\cos\phi-\cos\theta\cos\kappa\sin\phi \end{pmatrix} \begin{pmatrix} x \\ y \\ z \end{pmatrix}, \quad (12)$$

where κ, θ, and ϕ denote the Euler angles between the crystal and specimen coordinate systems. Stereographic projections of crystal orientations are shown in Fig. 2(c)-(e). These orientations are chosen so that z-component of slip direction and slip plane normal for the primary slip system of three grains vanish and the angles α between the tensile axis and slip direction of the primary system shown in Fig. 2(a) are 44° in the grain-1, -44° in the grain-2 and 46° in the grain-3. With this crystal orientation, the primary slip system under uniaxial load in y-direction is B4: $(11\bar{1})[101]$ and components $P_{ij}^{(B4)}$ of Schmid tensors for the primary systems in grains 1and 2 are

$$P_{ij}^{(B4)} = \begin{pmatrix} -0.4997 & \pm 0.0175 & 0 \\ \pm 0.0175 & 0.4997 & 0 \\ 0 & 0 & 0 \end{pmatrix}, \quad (13)$$

where plus and minus sign at the P_{12} (=P_{21}) component apply to the grains 1 and 2, respectively. Schmidt tensor for the primary system in the grain 3 is identical to that for the grain 2. Therefore, if we apply a uniaxial load in y-direction to grains 1, 2 or 3, individually, normal plastic strain components in the loading direction, and in the x-direction are the same for all the grains. At the same time, shear strains $\varepsilon_{yz}^{(p)}$, $\varepsilon_{zx}^{(p)}$ and the normal strain in z-direction are zero. Therefore, Eq. (3) shows that mutual constraint of deformation will not take place when

arbitrarily chosen two grains are welded and subjected to uniaxial load in *y*-direction. However, mutual constraint of deformation between crystal grains take place when the three grains are welded to each other and subjected to external tensile/compressive load in *y*-direction because of the difference in $P_{12}^{(B4)}$. In other words, uniform slip deformations on the primary system in three grains will lead to a deformation field analogous to Volterra disclination of wedge type [32].

The specimen is divided into eight-node finite elements. All the elements has the cubic shape with lateral dimension of 5 μm and the total number of elements for the model shown in Fig. 2(a) is 40 x 60 x 20. Effects of finite element mesh size was examined and confirmed elsewhere [16] that qualitative aspects of dislocation accumulation after cyclic loading were not influenced largely when the mesh size is smaller than 10% of the representative size of grains. In this study, we employ a mesh size which is 5% of the representative grain size 100 μm.

Displacement of the bottom end (surface at y=0) of the specimen is fixed in *y*-direction as shown in Fig. 2(b). A uniform tensile displacement in *y*-direction is given to the top end (surface at y=300 μm) while all the lateral surfaces are traction free.

4. Results and discussion

Fig. 3 shows analysis result of load-elongation relationship of the tricrystal specimen. Nominal tensile stress at the first yielding is about 0.8 MPa and after the first tensile deformation up to the nominal strain of 1%, which is designated by **A** in the Fig. 3, the flow stress is about 2.2 MPa. After the deformation to the stage **A**, external load is reversed to compression until the nominal tensile strain decreases to zero and this point of deformation stage is designated by **B**. The external load is reversed again to tensile deformation until the stage **C** is obtained. This cyclic-loading process is repeated three times and numerical data for GN dislocation densities and other quantities are recorded. Numerical data for load-elongation curve after the deformation stage **C** were sparsely recorded to reduce the size of numerical data. Because of this fact, the load-elongation curve after the deformation stage **C** is drawn by dotted lines showing that these lines do not give analysis results but just give an eye guide. Data shown by diamond shaped symbols indicate analysis results.

Distributions of shear strain and GN dislocation densities on slip systems on B4: $(11\bar{1})[101]$ and A3: $(111)[10\bar{1}]$ at the deformation stage **A** in the model shown in Fig. 2(a) are shown in Figs. 4(a)-(d). Figs. 4(e) and (f) show density distributions of GNDs on B4 and A3 slip systems in the modified specimen where the dimension of the grain-3 is extended in *y*-direction. Nominal tensile strain in this modified specimen is also 1%. As shown in Figs. 4(a) and (b),

slip deformation on the primary slip system is non-uniform near the grain boundary triple junction and slip on a secondary system of A3 evolve from the triple line. As a result of these non-uniform slip deformations, GN dislocations accumulate and make up some strip shaped regions with high density of GN dislocations in grain interiors. Fig. 4(c) shows density distribution of the edge component of GN dislocations on the primary system. Screw component of GNDs on the primary system is much smaller than the edge component (the data are shown later) and the high-density strips mostly consist of edge components of plus and minus signs. Directions of the high-density strips are approximately perpendicular to the slip planes. This means that edge dislocations line up to make kink-walls, or low angle grain boundaries inside grains, which is also schematically shown in Fig. 4(c). Magnitudes of the shear strain and GN dislocation density on the A3 slip system are relatively small compared to those on the primary system however, they show some peaks near the triple line. If we compare Figs. 4(c) and (e) or Figs. 4(d) and (f), it is clearly shown that the constraint condition imposed to the top surface (uniform tensile displacement in *y*-direction) has only a slight effect and the dislocation patterns are primarily developed by the interaction of three crystal grains. Therefore, we will focus our attention to the phenomena observed in the model shown in Fig. 2(a) in the following discussion.

Figs. 5(a)-(d) show distributions of shear strains and GND densities on slip systems B4 and A3 at the deformation stage **B**. Shear strains on slip systems do not vanish in grain interior and moreover, reverse slips take place at some regions. High-density strips of GN dislocations on the primary system change into diffused bands. If we compare Figs. 4(d) and 5(d), we notice that additional accumulation of GN dislocations on the A3 slip system takes place during the unloading process from the stage **A** to **B**.

Fig. 6 (a) and (b) show density distributions of GN dislocations at the deformation stage **C**. Distribution of GNDs on the primary system is more or less similar to that obtained at the deformation stage **A**, while the GNDs on the secondary system show some additional development as indicated by arrows in Fig. 6(b). Figs. 7(a) and (b) show density distributions of GNDs at the deformation stage **D**. Upon unloading to the deformation stage **D**, strip shaped structure of GNDs on the primary system is more developed compared to those observed in Fig 5(c) and the density distribution of GNDs on the secondary system show some growth, too. Density distributions of GNDs at the deformation stages **E** and **F** are shown in Figs. 8 and 9, respectively. Strip shaped structures of GNDs continue to develop with repetition of deformation cycles and some smaller strips of high-density regions are added.

In order to observe the development of GND structure with deformation cycles more quantitatively, density distributions of GNDs along path lines AA' and BB' shown in Fig. 2(a) are compared. Path lines AA' and BB' are situated 7.5 μm above and beneath the grain

boundaries and thread the center of the thickness (z=5μm) of the specimen.

Figures 10(a) and (b) show density distributions of edge and screw components of GNDs on the primary slip system and along the path line AA', respectively. As shown in Fig. 10(a), the edge component changes its sign at tensile and compressive loading stages and the density gradually increases with repeated loading cycles. Peak values at tensile stages **C** and **E** do not show significant change, while the peak values at zero-strain stages **B**, **D** and **F** steadily increase. Screw component of GNDs plotted in Fig. 10(b) shows that the density is one-order smaller than that of edge component, indicating that the strip patterns shown in Fig. 4(c) and others consist of almost-pure edge dislocations.

Figures 11(a) and (b) show density distributions of edge and screw components of GNDs on the primary slip system and along the path line BB', respectively. The peak values of the edge component at deformation stages **A**, **C** and **E** do not show significant change, while the peak values at stages **B**, **D** and **F** increase gradually. Screw component of GNDs is small compared to that of edge component and its growth with deformation cycles is very small.

Figures 12(a) and (b) show edge and screw components of GNDs on the secondary slip system A3 and along the path line AA', respectively. In contrast to the results obtained in Figs. 10(a) and 11(a), edge component on this slip system does not change sign at the tensile and zero-strain deformation stages. Density values at the largest peaks shown in Figs. 12(a) and (b) do not show significant change during three cycles of deformation and this mean that this structure of GNDs is stable in the microstructure. It is also noted that small peaks, indicated by arrows in Figs. 12(a) and (b), are formed after the first tensile deformation. These peaks are stable, too.

Figures 13(a) and (b) show density distribution of edge and screw components of GNDs on the A3 slip system and along the path line BB', respectively. Two peaks develop after the deformation stage **B** and they are stable, although the density value is much smaller compared to that generated on the primary slip system. It should be noted that these peaks are not generated during the first step of tensile deformation but formed upon reverse loading process and thereafter stable during repeated deformation cycles.

Although the GND density on the secondary slip system of A3 is very small compared to that on the primary system of B4, it is considered that dislocations on the A3 system play crucial roles in the evolution of dislocation pattern in the microstructure because dislocations on secondary slip system(s) interact with moving dislocations on the primary system, make entanglement of dislocations and shorten the mean free path of dislocations on the primary system. In the present case, interaction of dislocations on B4 and A3 slip systems will result in the formation of Hirth lock [20]. In general, these elementary processes of dislocation entanglement will lead to localized hardening and dislocation patterning in the microstructure.

Figures 14(a) and (b) show density distributions of SSDs on the primary system B4 when the deformation stages are at **C** and **E**, respectively. Some strip shaped regions develop into grain interiors from the triple junction and their direction and extension show that the accumulation of SSDs on the B4 slip system have a close relation to the accumulation of GNDs on the secondary slip system of A3 rather than those on the primary system of B4. This shows that strip shaped regions of dislocation entanglement, or at least co-existence of dislocations on more than one system, are formed. The density of SSDs is one order higher than that of GNDs. This is partly because the size of crystal grains is relatively large. Smaller grain size will result in higher density of GNDs while densities of SSDs will not change largely and this will result in different development of dislocation patterns. Comparison of Fig. 14(a) and (b) shows that spatial pattern of SSDs does not change largely with repetition of loading while the density increases. If the cyclic deformation continues, the density of SSDs will increase at first and then saturate due to the mechanism of pair annihilation of dislocations with opposite sign, on which further study is needed. Figure 15(a) and (b) show histograms of dislocation mean free path on slip systems B4 and A3, respectively. At the deformation stage **A**, the mean free path on the B4 slip system stays at the initial value of 158 μm in about 50 % volume of the specimen, while in the remaining part of the specimen, the mean free path is slightly shortened due to the superimpose of slip activity on A3 and other systems. In contrast to this, the mean free path on the A3 system (Fig. 15(b)) is largely shortened and distribute at about 20 μm. At the deformation stage **C**, the mean free paths on the slip systems B4 and A3 show significant decreases from those at the stage **A**. Changes from the deformation stage **C** to **E** is relatively moderate. This is considered to show that structure of dislocations gradually stabilize with repeated loading.

Another factor to be considered is the combination of crystal orientations. The tricrystal model employed in this study has disagreement only in the Schmid tensor component P_{12} between grains and all the other components are identical for three grains. If another component of the Schmid tensor disagrees between grains, another deformation field will develop. For example, disagreement of P_{13} components between grains 1 and 2 will induce a deformation field analogous to the Volterra's disclination of screw type [18], while disagreement of P_{22} component between grains 1 and 2 will result in non-uniform slip deformation along the grain boundary plane [17] and different dislocation structure will develop.

Some dislocation structures formed after the first reversal of loading were stable during the following cycles of deformation. It is not yet clear whether these structures are stable under a much larger number of cyclic deformations. Also, it is not yet known how often such stable structures are formed in polycrystalline microstructure.

Although the crystal orientations of the employed tricrystal model are highly controlled ones to simplify the slip phenomena, analysis results are believed to predict important features taking place in polycrystalline microstructure. Fig. 16(a)-(c) shows analysis results of GND distributions in a six-grained multicrystal model subjected to a monotonic tensile load in *y*-direction [28,33]. Angles between grain boundaries are neither 90° nor 180°, but they are closer to 120°. Orientations of the constituent grains were randomly chosen inside the stereographic triangle of [100]-[110]-[111] and this multicrystal model is more realistic than that shown in Fig. 2 in terms of the geometry of crystal grains and their crystal orientations.

It is observed that GNDs not only pile-up at some grain boundary planes, but also a lot of high-density strip regions evolve into grain interior from grain boundary triple junctions. In other words, evolution of high-density strip regions of GNDs from triple junctions is not limited to take place in the tricrystal specimen with controlled geometry but rather generally observed phenomenon in polycrystal microstructure[*]. It is also interesting to note that these high-density strip regions shown in Fig. 16 are more or less curved, while the high-density strip regions in the tricrystal specimen looks to be straight, as shown in Figs. 4-9. This difference is considered to reflect the difference in stress distribution in the specimens. That is, the onset of slip deformation immediately induces a non-uniform distribution of stresses however, the stress distribution in the tricrystal specimen is relatively simple. On the other hand, the one in the six-grained specimen is much more complex due to the superposition of effects arising from more than two triple junctions. Some of these structures of GNDs will repeat the growth and degradation upon reversal of the applied stress and gradually develop into a more defined pattern as we observed in Figs. 4-9, while other structure will be stable under repeated loading. Moving dislocations which are responsible for the realization of macroscopic plastic deformation are assumed to be entangled to high density regions of dislocations [2],[3] which consist of GNDs and SSDs, and stronger structure will be gradually established.

5. Summary

Cyclic plastic slip deformation of a tricrystal model where crystal orientations of constituent

[*] High density accumulation of dislocations in strip shaped regions is experimentally observed even in single crystals [33]. The strip shaped region is formed from initial inhomogeneity and extends in direction perpendicular to the slip direction due to a slight deviation from uniaxial stress state after a certain amount of slip [34]. Although the high density strip of dislocations in single crystals are relatively moderate compared to those observed in multicrystal models, it is considered that the formation of these strip shaped region will serve as s basis for the formation of dislocation patterned structure during cyclic deformation.

grains were carefully chosen to control the mechanical interaction was evaluated by a finite element based-crystal plasticity analysis and evolution of the geometrically necessary dislocations was discussed. Results are summarized as follows.

1. High-density strips of the geometrically necessary dislocations (GNDs) on the primary slip systems were formed from grain boundary triple junction and evolved into grain interiors. Character of the GNDs was almost pure edge type and changed their sign with tensile and compressive loading stages.
2. Accumulation of GNDs on a secondary slip system was also observed. GNDs on the secondary system did not change character upon reversal of external load, even though the density was about one order smaller than that on the primary system. It was noted that some structures evolved during the first reversal of the external load and they were stable during the following three cycles of deformation.

References

[1] O.B. Pedersen, in:, J. et al Lepinoux (Ed.), Multiscale Phenomena in Plasticity: From Experiments to Phenomenology, Modelling and Materials Engineering, Kluwer Academic Press, Dordrecht, 2000, pp. 83-97.

[2] H. Mughrabi, Acta Metallurgica 31 (1983) 1367-1379.

[3] D. Walgraef, E.C. Aifantis, Journal of Applied Physics 58 (1985) 688-691.

[4] C. Buque, J. Bretschneider, A. Schwab, C. Holste, Materials Science and Engineering: A 300 (2001) 254-262.

[5] A. Franěk, R. Kalus, J. Kratochvíl, Philosophical Magazine A 64 (1991) 497-511.

[6] J. Kratochvíl, Czechoslovak Journal of Physics 38 (1988) 421-424.

[7] R. Madec, B. Devincre, L.P. Kubin, Scripta Materialia 47 (2002) 689-695.

[8] T. Fujii, C. Watanabe, Y. Nomura, N. Tanaka, M. Kato, Materials Science and Engineering: A 319-321 (2001) 592-596.

[9] Z.F. Zhang, Z.G. Wang, Philosophical Magazine Letters 78 (1998) 105-113.

[10] R.T.T. Dehoff, F.N. Rhines, Quantitative Microscopy, McGraw-Hill., New York. US., 1968.

[11] R. Hook, J. Hirth, Acta Metallurgica 15 (1967) 535-551.

[12] R. Hook, J. Hirth, Acta Metallurgica 15 (1967) 1099-1110.

[13] J.P. Hirth, Metallurgical Transactions 3 (1972) 3047-3067.

[14] J.J. Hauser, B. Chalmers, Acta Metallurgica 9 (1961) 802-818.

[15] R. Kondou, T. Ohashi, JSME International Journal A49 (2006) 581-588.

[16] T. Mayama, T. Ohashi, R. Kondou, International Journal of Plasticity 25 (2009) 2122-2140.

[17] T. Ohashi, Colloque De Physique 51 (1990) C1-593-598.

[18] T. Ohashi, M. Sato, Y. Shimazu, Materials Science Forum 654-656 (2010) 1283-1286.

[19] R. Kondou, T. Ohashi, Key Engineering Materials 340-341 (2007) 187-192.

[20] T. Ohashi, Philosophical Magazine A 70 (1994) 793-803.

[21] T. Ohashi, Philosophical Magazine Letters 75 (1997) 51-57.

[22] T. Ohashi, International Journal of Plasticity 21 (2005) 2071-2088.

[23] R. Hill, Journal of the Mechanics and Physics of Solids 14 (1966) 95.

[24] N. Fleck, G. Muller, M. Ashby, J. Hutchinson, Acta Metallurgica Et Materialia 42 (1994) 475-487.

[25] J. Weertman, Acta Materialia 50 (2002) 673-689.

[26] I. Hayashi, M. Sato, M. Kuroda, Journal of the Mechanics and Physics of Solids 59 (2011) 1731-1751.

[27] T. Ohashi, Trans. JIM 28 (1987) 906-915.

[28] T. Ohashi, in:, H. Kitagawa, Y. Shibutani (Eds.), IUTAM Symposium on Mesoscopic Dynamics of Fracture Process and Materials Strength, Kluwer Academic Press, Osaka, Japan, 2003, pp. 97-106.

[29] D. Kuhlmann-Wilsdorf, Materials Science and Engineering: A 113 (1989) 1-41.

[30] D. Kuhlmann-Wilsdorf, Metallurgical Transactions A16 (1985) 2091.

[31] T. Ohashi, R.I.I. Barabash, J.W.L.W.L. Pang, G.E.E. Ice, O.M.M. Barabash, International Journal of Plasticity 25 (2009) 920-941.

[32] J.P. Hirth, J. Lothe, Theory of Dislocations, 2nd ed., John Wiley & Sons, New York. US., 1982.

[33] K. Higashida, T. Ohashi, in:, K. Higashida, N. Tsuji (Eds.), Proc. 2nd Int. Symp. Steel Science (ISSS2009), The Iron and Steel Institute of Japan, Kyoto, Japan, 2009, pp. 15-26.

[34] T. Ohashi, Materials Transactions, JIM 31 (1990) 456-462.

Table 1 Material constants and crystal orientations employed in this study

Grain	Elastic compliance [10^{-11} Pa^{-1}]			Magnitude of Burgers Vector [10^{-10}m]	Euler angles [Deg.]		
	S_{11}	S_{12}	S_{44}	$\tilde{b}$	κ	θ	ϕ
1	1.0	-0.25	2.5	2.556	74.98	24.53	79.47
2	↑	↑	↑	↑	↑	↑	259.47
3	↑	↑	↑	↑	79.65	24.97	75.24

Figure captions

Fig. 1 Calculated stress–strain curves of single crystals which are tensile deformed in S and D orientations. Specimens are assumed to be perfectly uniform and single and double slip deformation take place uniformly.

Fig. 2 Tricrystal specimen employed in this study. (a) Specimen geometry and schematic illustration of the primary slip system in each crystal grain, (b) Loading and boundary condition, (c)-(e) Stereographic projection of crystal orientation of grain-1, -2 and -3, respectively. In (c)-(e), slip plane normal directions and slip directions for the primary and a secondary (critical) systems are indicated by filled and open symbols, respectively.

Fig. 3 Load-elongation relationship for three-cycles of deformation. Range of the nominal tensile strain is 0-1%.

Fig. 4 Distributions of plastic shear strain and the density of geometrically necessary dislocations at the deformation stage **A**. Nominal strain and stress are 0.01 and 2.19 MPa, respectively. (a) and (b); plastic shear strain on the primary (B4:(11-1)[101]) and a secondary (A3:(111)[10-1]) slip systems, (c) and (d); density distributions of $\rho_{G,edge}^{(B4)}$ and $\left\|\rho_G^{(A3)}\right\|$, respectively. (e) and (f); density distributions of $\rho_{G,edge}^{(B4)}$ and $\left\|\rho_G^{(A3)}\right\|$, respectively in a tricrystal specimen where the dimension in *y*-direction of the grain-3 is double the model shown in Fig. 2(a).

Fig. 5 Distributions of plastic shear strain and the density of geometrically necessary dislocations at the deformation stage **B**. Nominal strain and stress are 0 and -2.83 MPa, respectively. (a) and (b); plastic shear strain on the primary (B4: $(11\bar{1})[101]$) and a secondary (A3: $(111)[10\bar{1}]$) slip systems, (c) and (d); density distributions of $\rho_{G,edge}^{(B4)}$ and $\left\|\rho_G^{(A3)}\right\|$, respectively.

Fig. 6 Density distributions of the geometrically necessary dislocations at the deformation stage **C**. Nominal strain and stress are 0.01 and 3.33 MPa, respectively. (a) $\rho_{G,edge}^{(B4)}$ and (b)

$\left\|\rho_G^{(A3)}\right\|$. Comparison of (b) with Fig. 4(d) shows that distribution of GNDs are newly added at sites indicated by arrows.

Fig. 7 Density distributions of the geometrically necessary dislocations at the deformation stage **D**. Nominal strain and stress are 0 and -3.75 MPa, respectively. (a) $\rho_{G,edge}^{(B4)}$ and (b) $\left\|\rho_G^{(A3)}\right\|$.

Fig. 8 Density distributions of the geometrically necessary dislocations at the deformation stage **E**. Nominal strain and stress are 0.01 and 4.13 MPa, respectively. (a) $\rho_{G,edge}^{(B4)}$ and (b) $\left\|\rho_G^{(A3)}\right\|$.

Fig. 9 Density distributions of the geometrically necessary dislocations at the deformation stage **F**. Nominal strain and stress are 0 and -4.47 MPa, respectively. (a) $\rho_{G,edge}^{(B4)}$ and (b) $\left\|\rho_G^{(A3)}\right\|$.

Fig. 10 Density distributions of (a) edge and (b) screw components of the GNDs on the primary slip system and along the line AA' shown in Fig. 2(a).

Fig. 11 Density distributions of the (a) edge and (b) screw components of the GNDs on the primary slip system and along the line BB' shown in Fig. 2(a).

Fig. 12 Density distributions of (a) edge and (b) screw components of the GNDs on the A3 slip system and along the line AA' shown in Fig. 2(a).

Fig. 13 Density distributions of the (a) edge and (b) screw components of GNDs on the A3 slip system and along the line BB' shown in Fig. 2(a).

Fig. 14 Density distributions of the statistically stored dislocations on the B4 slip system and at the deformation stages **C** (a), and **E** (b).

Fig. 15 Histograms of the dislocation mean free path for slip systems B4 (a), and A3 (b). At the deformation stage **A**, the mean free path on the B4 slip system is 158-159 μm in about 50 % volume of the tricrystal specimen. The mean free path on the A3 slip system and at deformation stages **A**, **C** and **E** are close to 20, 11 and 9 μm, respectively, in the entire region of the specimen, while slip on this system takes in a small fraction of the volume.

Fig. 16 Distribution of the density norm of GNDs on (a) B4: $(11\bar{1})[101]$, (b) A3: $(111)[10\bar{1}]$, (c) C1: $(1\bar{1}1)[110]$ slip systems in a six-grained multicrystal specimen [28,33]. Dimension of the specimen is 5x15x1 μm. The specimen was monotonically tensile deformed in *y*-direction and the nominal strain was 1%.

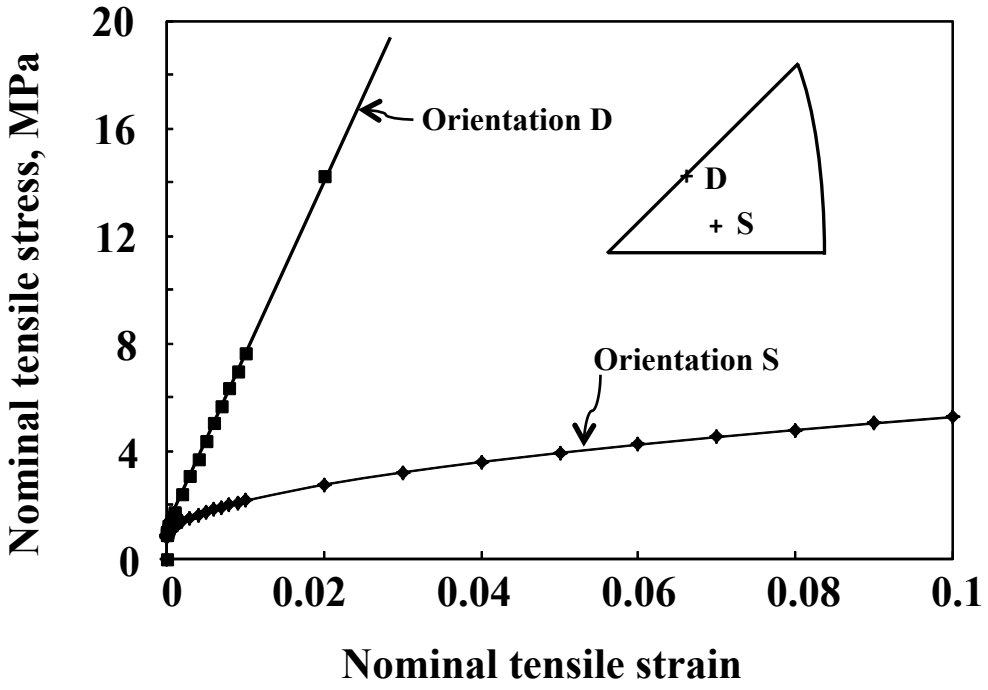

Fig. 1 Calculated stress–strain curves of single crystals which are tensile deformed in S and D orientations. Specimens are assumed to be perfectly uniform and single and double slip deformation take place uniformly.

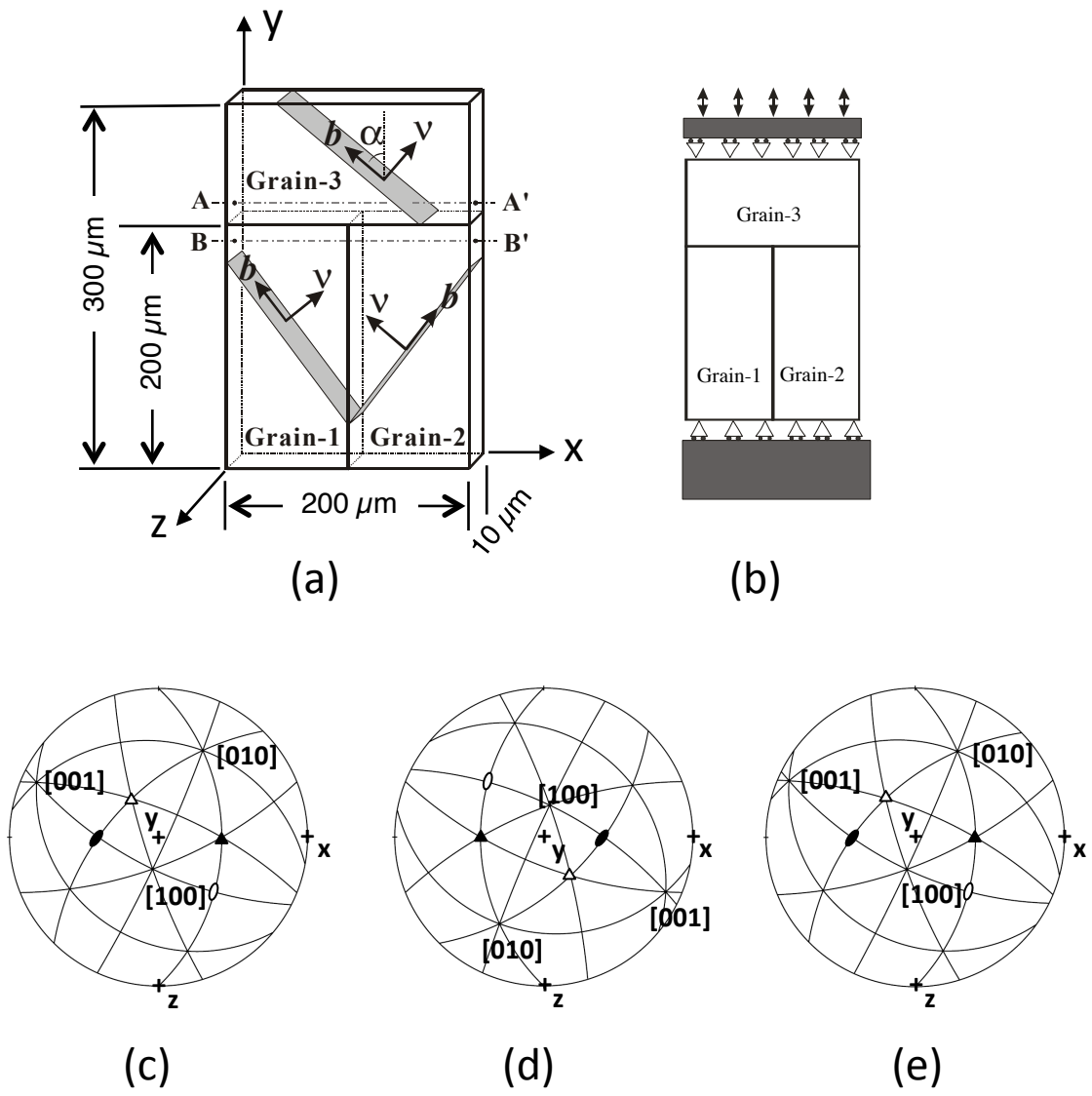

Fig. 2 Tricrystal specimen employed in this study. (a) Specimen geometry and schematic illustration of the primary slip system in each crystal grain, (b) Loading and boundary condition, (c)-(e) Stereographic projection of crystal orientation of grain-1, -2 and -3, respectively. In (c)-(e), slip plane normals and slip directions for the primary and a secondary (critical) systems are indicated by filled and open symbols, respectively.

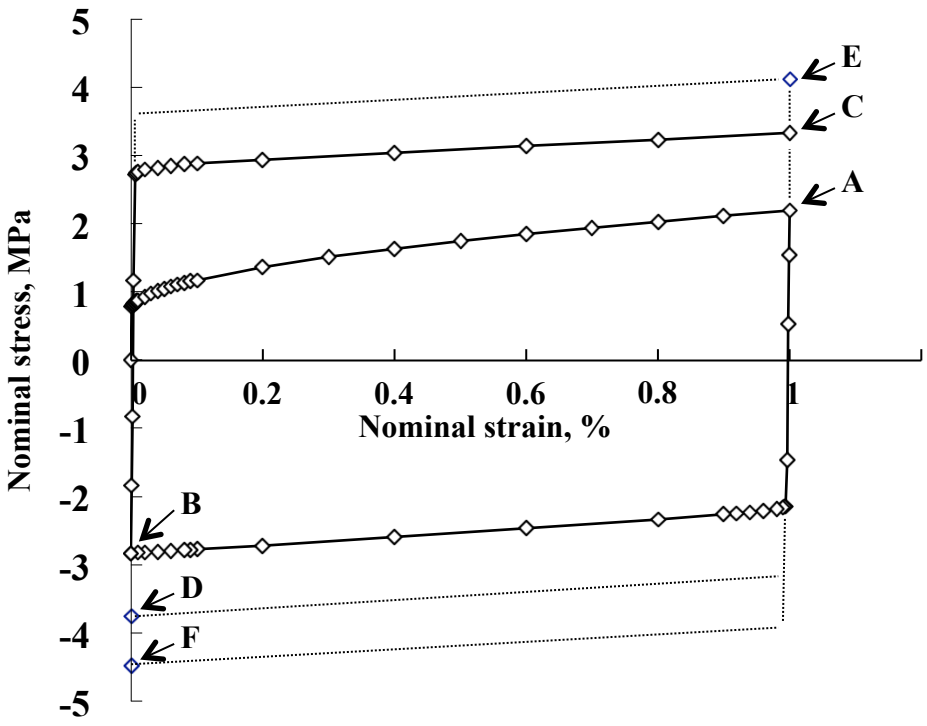

Fig. 3 Load-elongation relationship for three-cycles of deformation. Range of the nominal tensile strain is 0-1%.

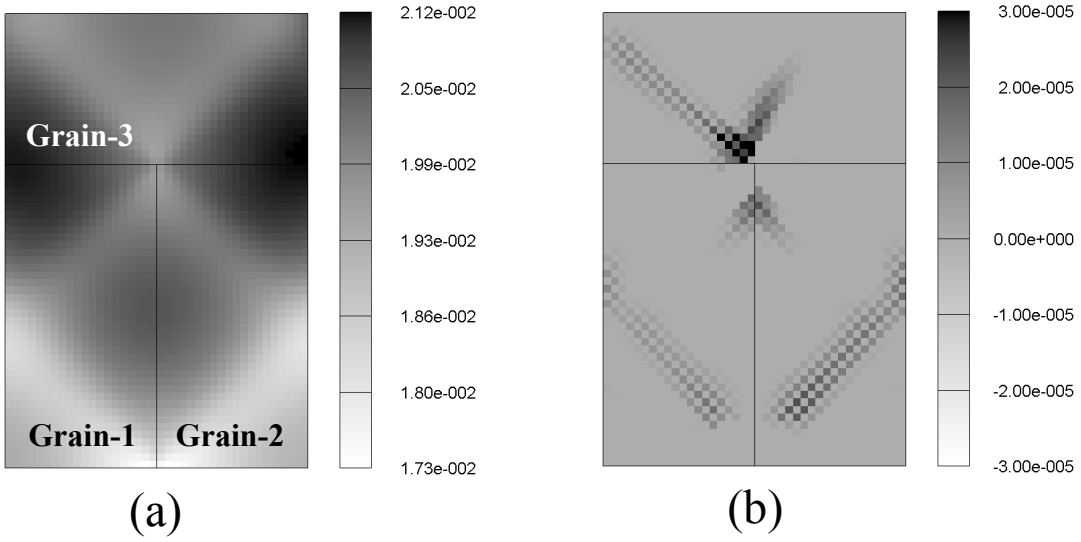

Fig. 4 Distributions of plastic shear strain and the density of geometrically necessary dislocations at the deformation stage **A**. Nominal strain and stress are 0.01 and 2.19 MPa, respectively. (a) and (b); plastic shear strain on the primary (B4:(11-1)[101]) and a secondary (A3:(111)[10-1]) slip systems, (c) and (d); density distributions of $\rho_{G,edge}^{(\mathrm{B4})}$ and $\left\|\rho_G^{(A3)}\right\|$, respectively. (e) and (f); density distributions of $\rho_{G,edge}^{(\mathrm{B4})}$ and $\left\|\rho_G^{(A3)}\right\|$, respectively in a tricrystal specimen where the dimension in *y*-direction of the grain-3 is double the model shown in Fig. 2(a).

continued to the next page

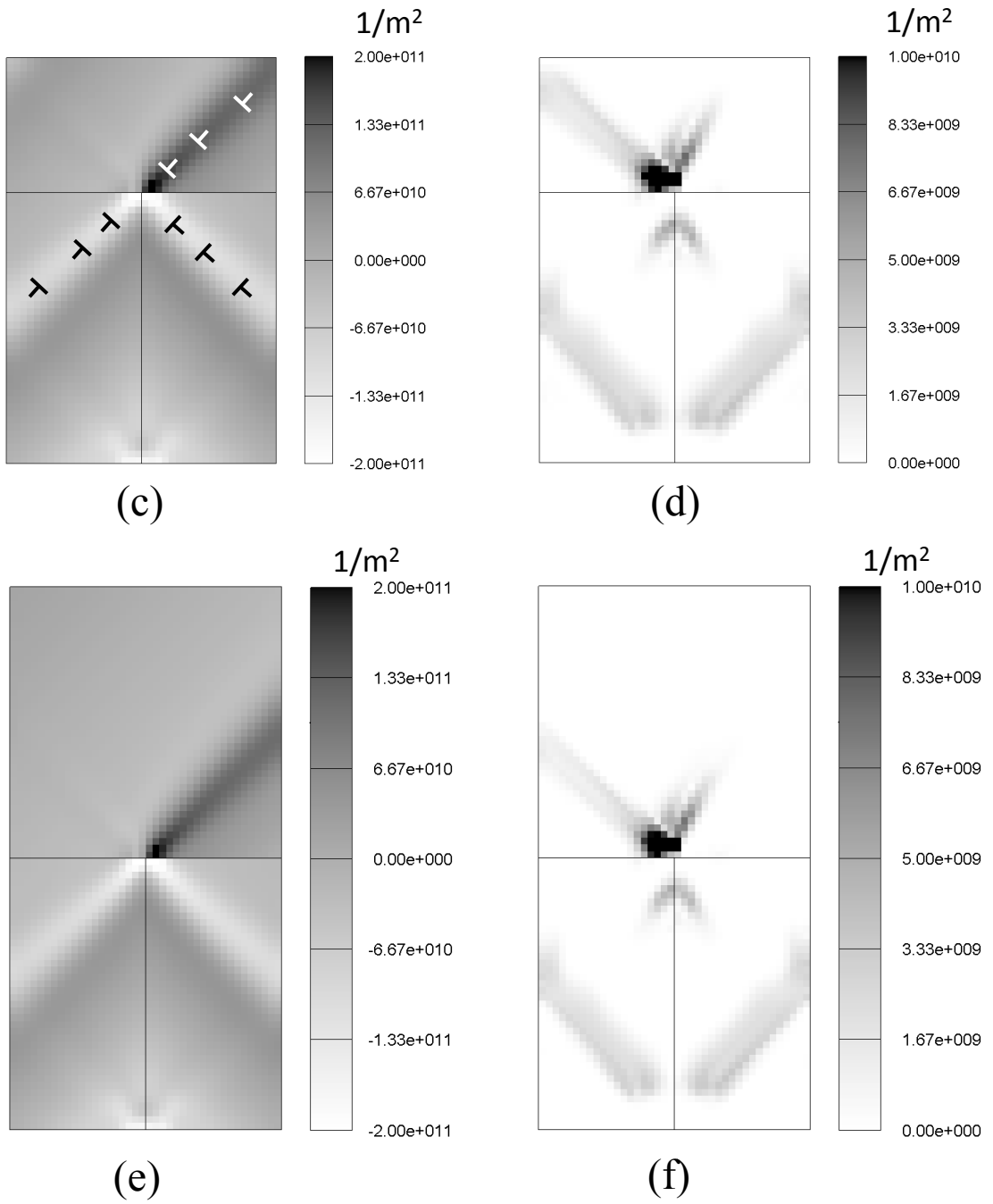

Fig. 4 Distributions of plastic shear strain and the density of geometrically necessary dislocations at the deformation stage **A**. Nominal strain and stress are 0.01 and 2.19 MPa, respectively. (a) and (b); plastic shear strain on the primary (B4:(11-1)[101]) and a secondary (A3:(111)[10-1]) slip systems, (c) and (d); density distributions of $\rho_{G,edge}^{(\mathrm{B4})}$ and $\left\|\boldsymbol{\rho}_G^{(A3)}\right\|$, respectively. (e) and (f); density distributions of $\rho_{G,edge}^{(\mathrm{B4})}$ and $\left\|\boldsymbol{\rho}_G^{(A3)}\right\|$, respectively in a tricrystal specimen where the dimension in *y*-direction of the grain-3 is double the model shown in Fig. 2(a).

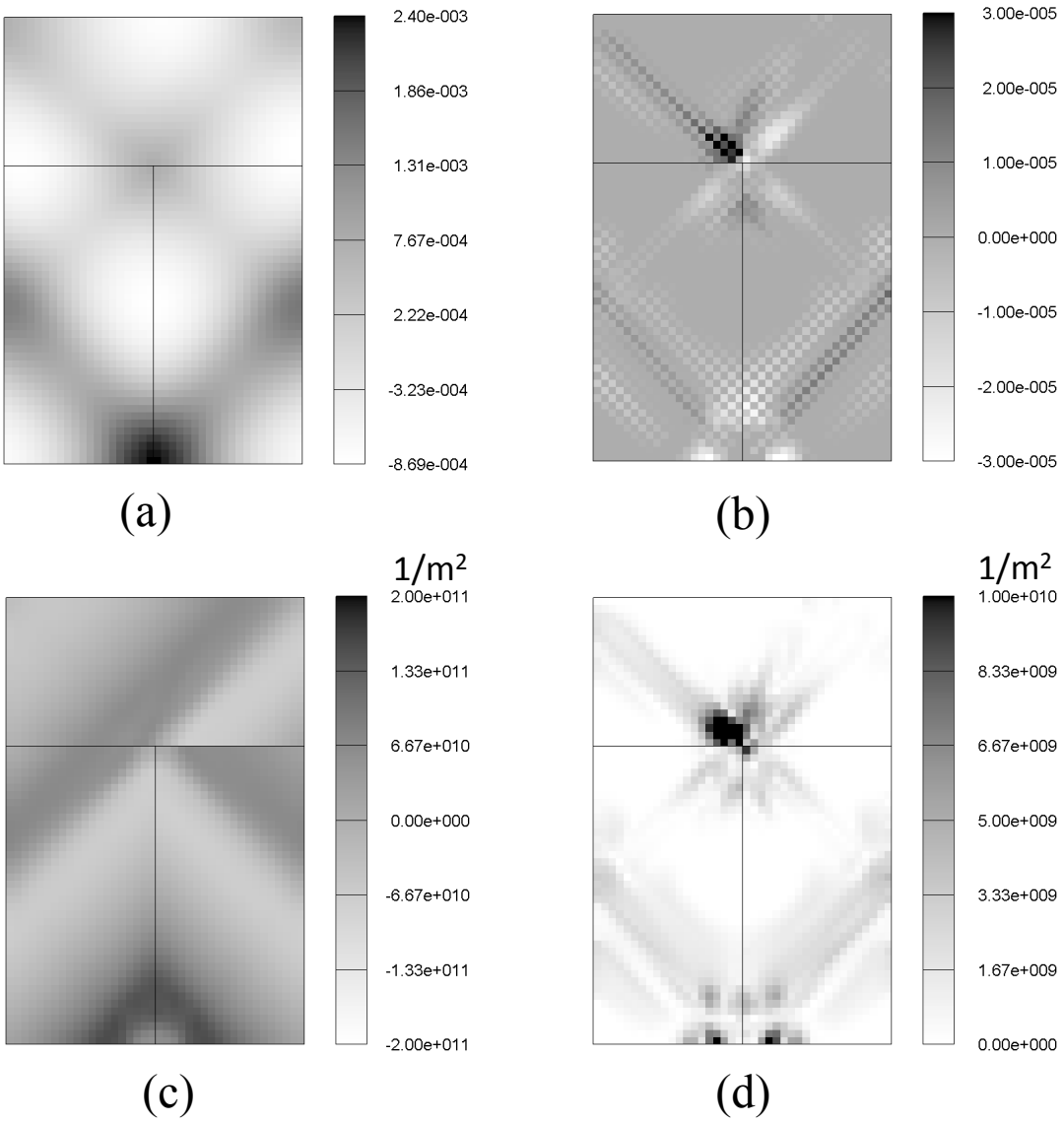

Fig. 5 Distributions of plastic shear strain and the density of geometrically necessary dislocations at the deformation stage **B**. Nominal strain and stress are 0 and -2.83 MPa, respectively. (a) and (b); plastic shear strain on the primary (B4:(11-1)[101]) and a secondary (A3:(111)[10-1]) slip systems, (c) and (d); density distributions of $\rho_{G,edge}^{(\mathrm{B4})}$ and $\left\|\rho_G^{(A3)}\right\|$, respectively.

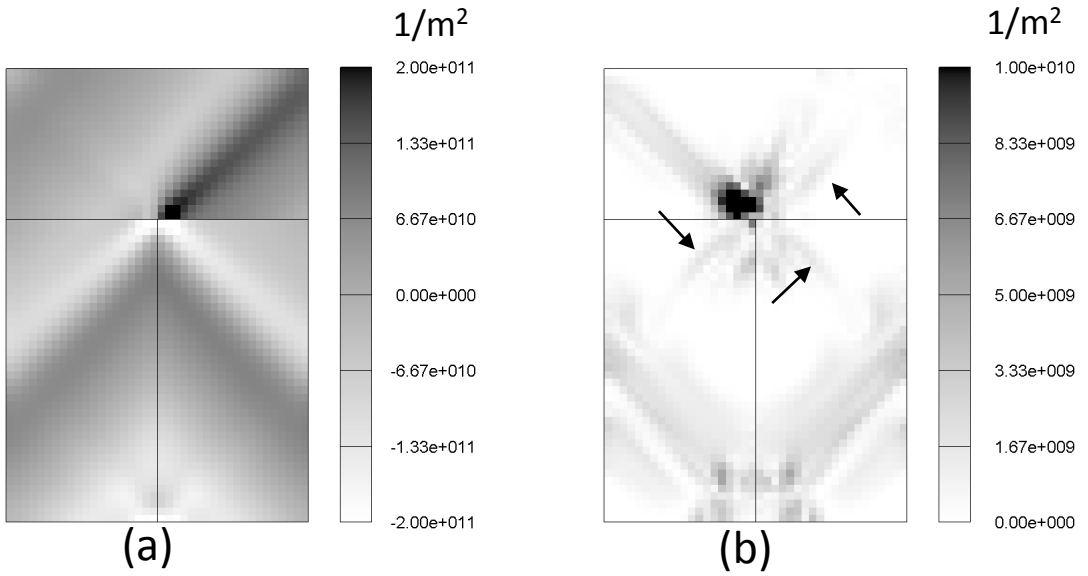

Fig. 6 Density distributions of the geometrically necessary dislocations at the deformation stage **C**. Nominal strain and stress are 0.01 and 3.33 MPa, respectively. (a) $\rho_{G,edge}^{(B4)}$ and (b) $\left\|\rho_G^{(A3)}\right\|$. Comparison of (b) with Fig. 4(d) shows that distribution of GNDs are newly added at sites indicated by arrows.

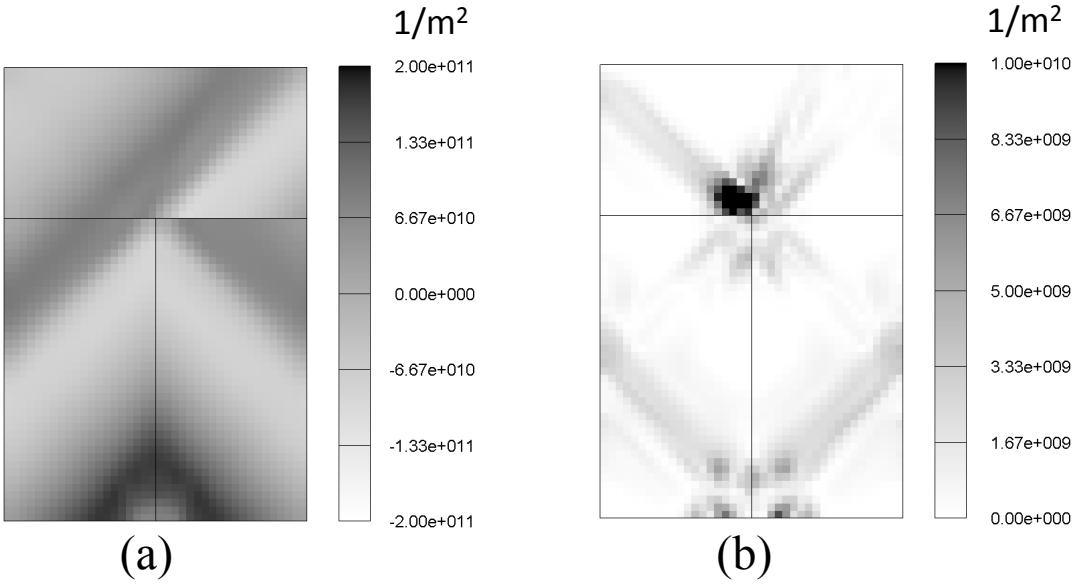

Fig. 7 Density distributions of the geometrically necessary dislocations at the deformation stage **D**. Nominal strain and stress are 0 and -3.75 MPa, respectively. (a) $\rho_{G,edge}^{(B4)}$ and (b) $\left\|\rho_G^{(A3)}\right\|$.

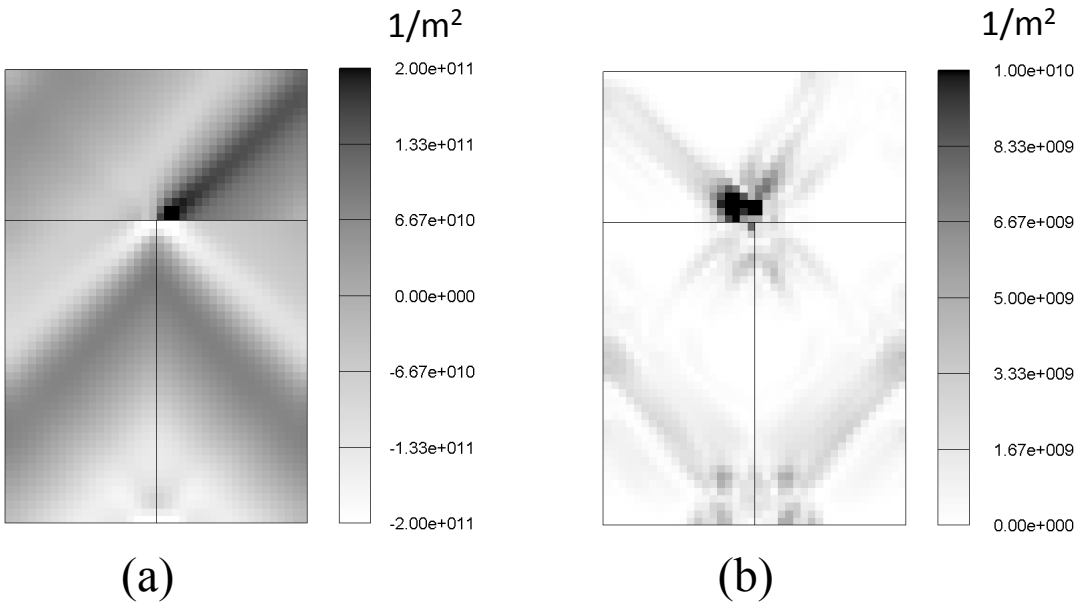

Fig. 8 Density distributions of the geometrically necessary dislocations at the deformation stage **E**. Nominal strain and stress are 0.01 and 4.13 MPa, respectively. (a) $\rho_{G,edge}^{(B4)}$ and (b) $\left\|\boldsymbol{\rho}_{G}^{(A3)}\right\|$.

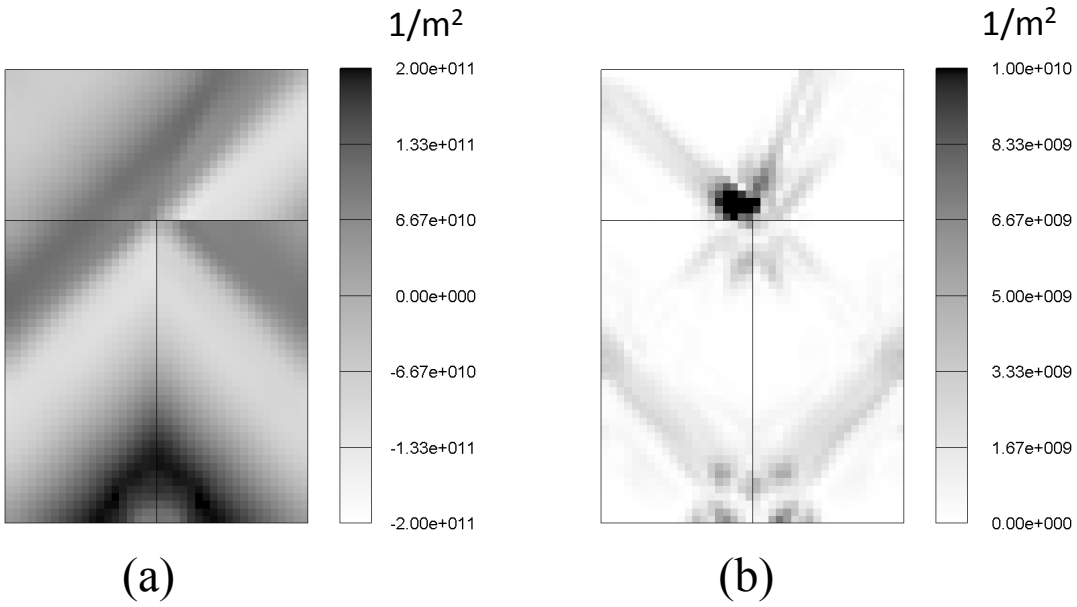

Fig. 9 Density distributions of the geometrically necessary dislocations at the deformation stage **F**. Nominal strain and stress are 0 and -4.47 MPa, respectively. (a) $\rho_{G,edge}^{(B4)}$ and (b) $\left\|\rho_G^{(A3)}\right\|$.

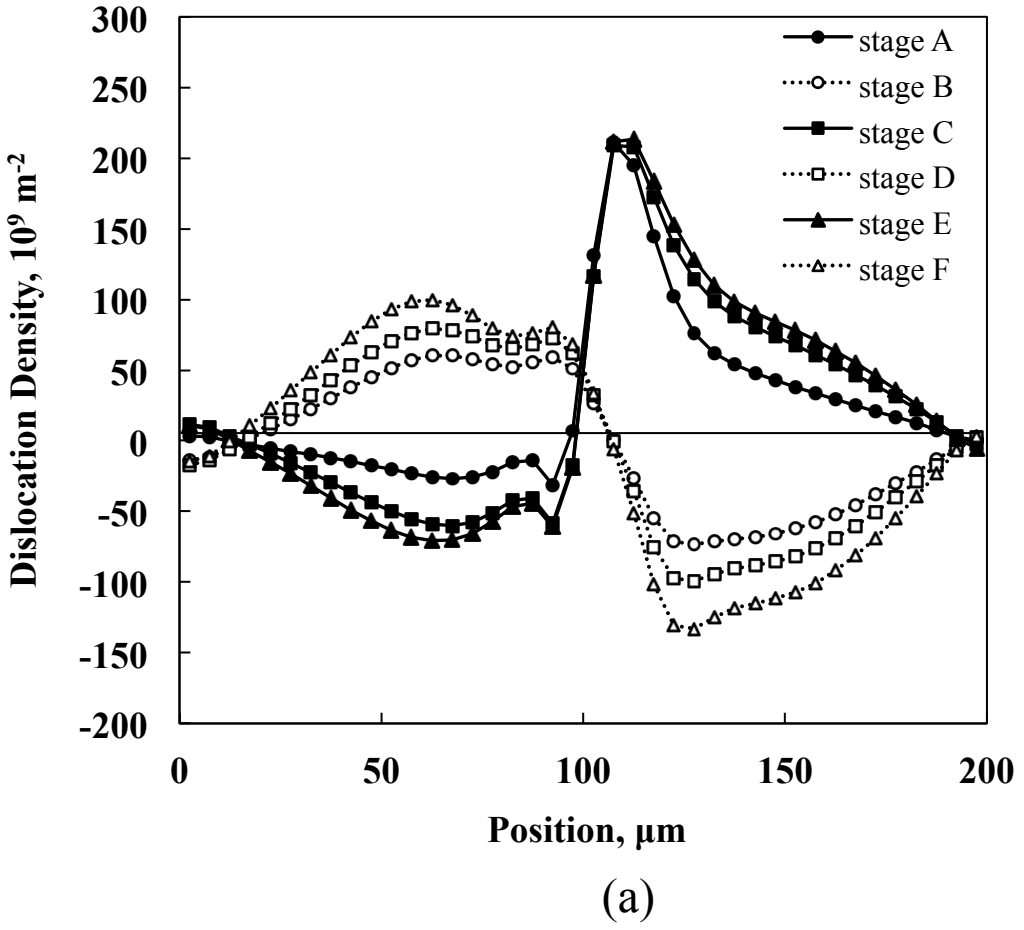

(a)

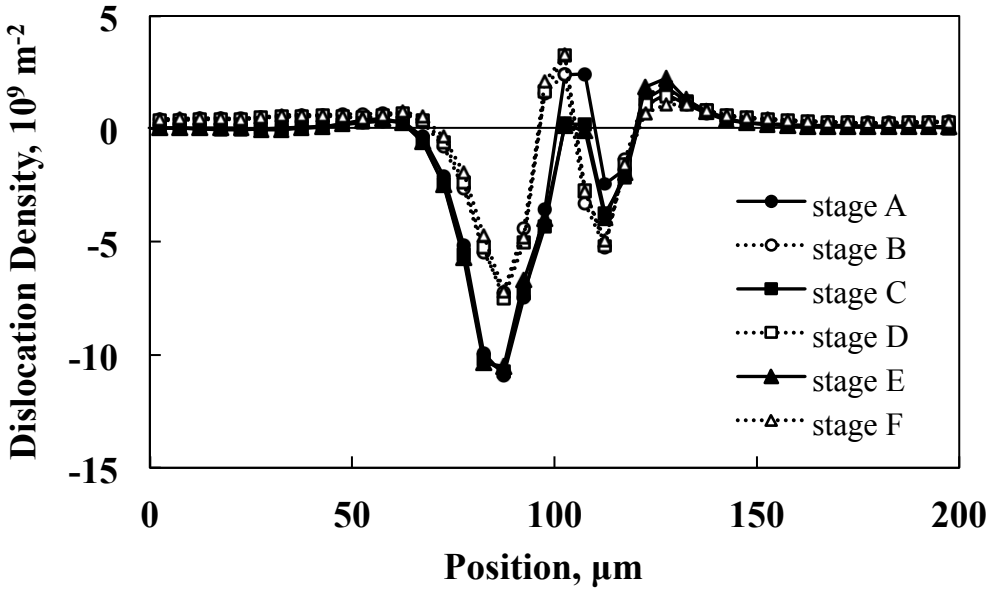

(b)

Fig. 10 Density distributions of (a) edge and (b) screw components of the GNDs on the primary slip system and along the line AA' shown in Fig. 2(a).

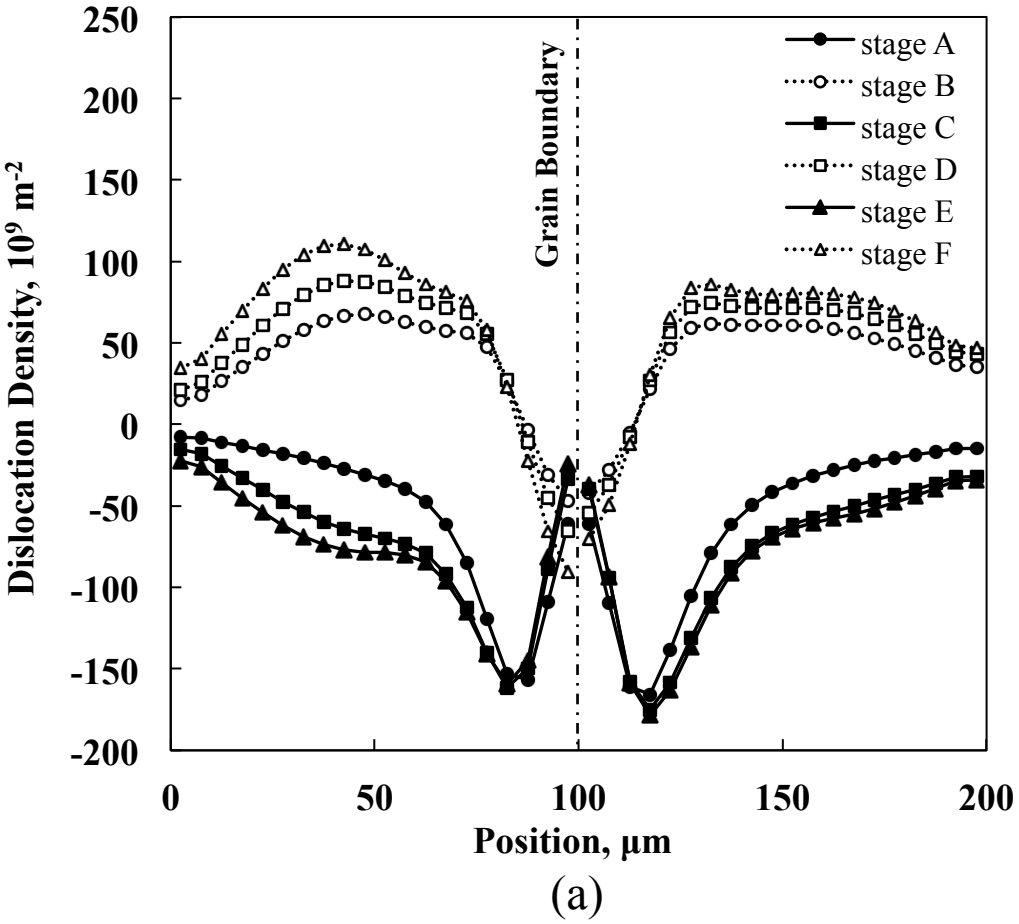

(a)

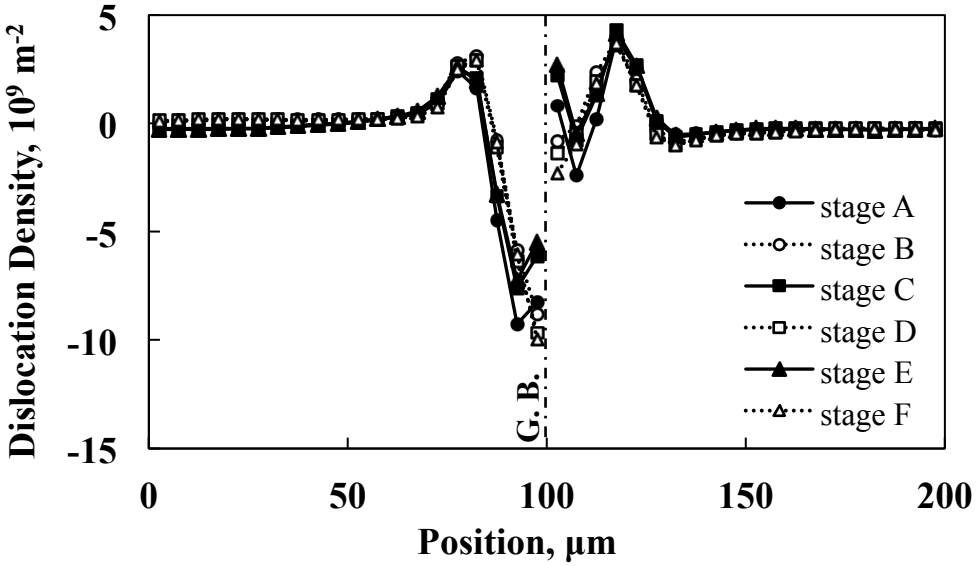

(b)

Fig. 11 Density distributions of the (a) edge and (b) screw components of the GNDs on the primary slip system and along the line BB' shown in Fig. 2(a).

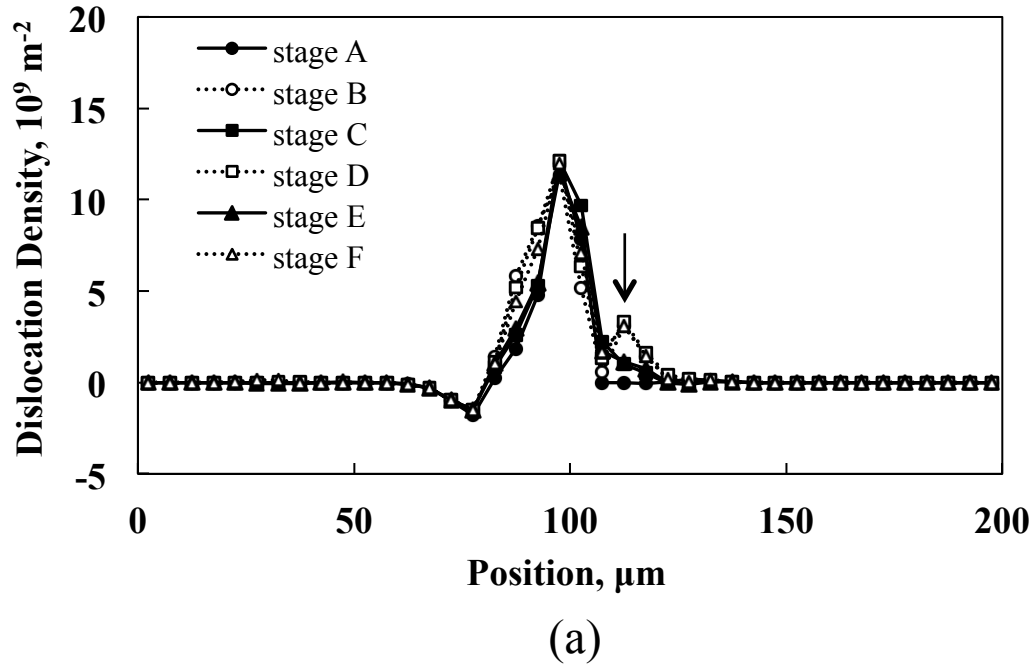

(a)

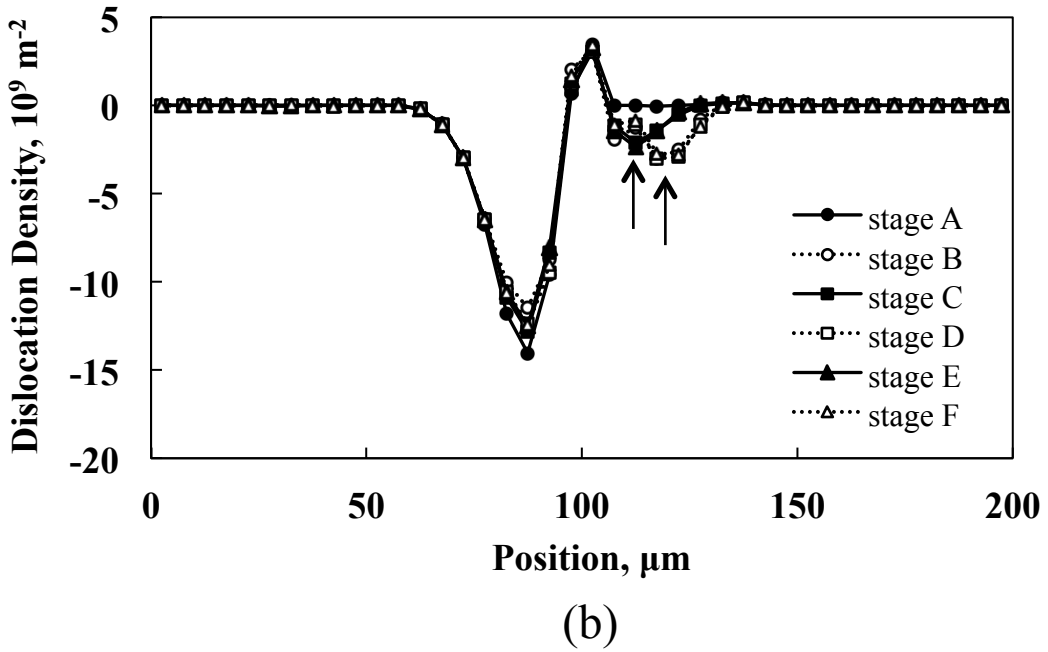

(b)

Fig. 12 Density distributions of (a) edge and (b) screw components of the GNDs on the A3 slip system and along the line AA' shown in Fig. 2(a).

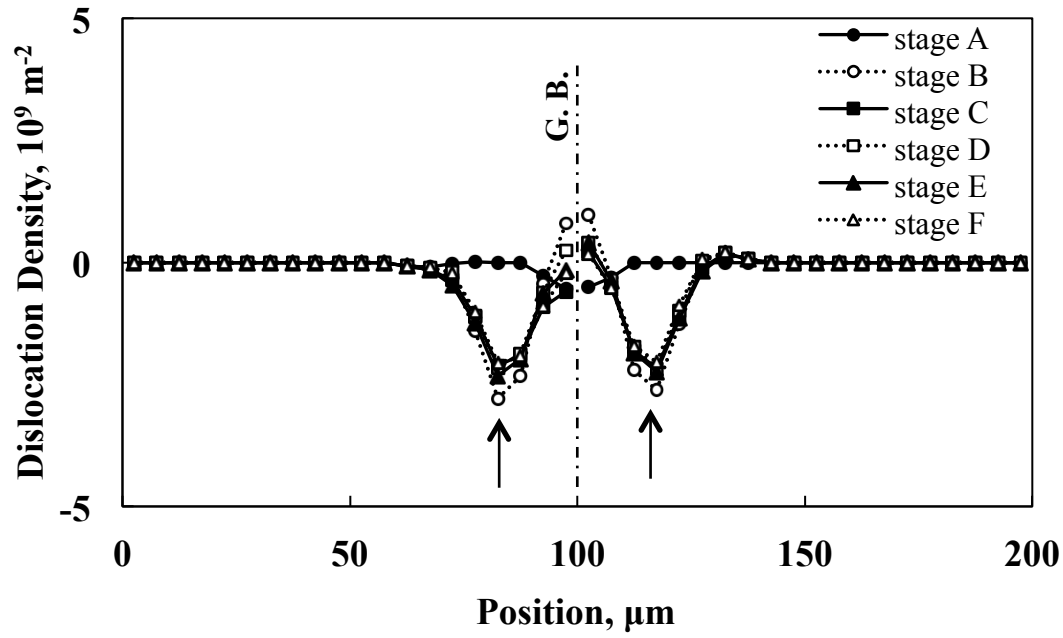

(a)

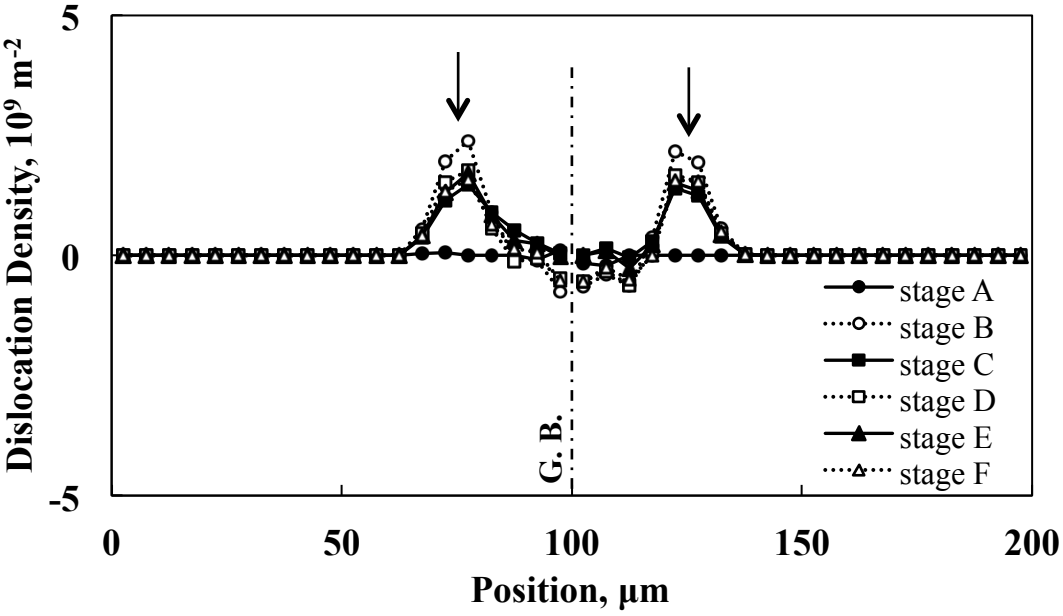

(b)

Fig. 13 Density distributions of the (a) edge and (b) screw components of GNDs on the A3 slip system and along the line BB' shown in Fig. 2(a).

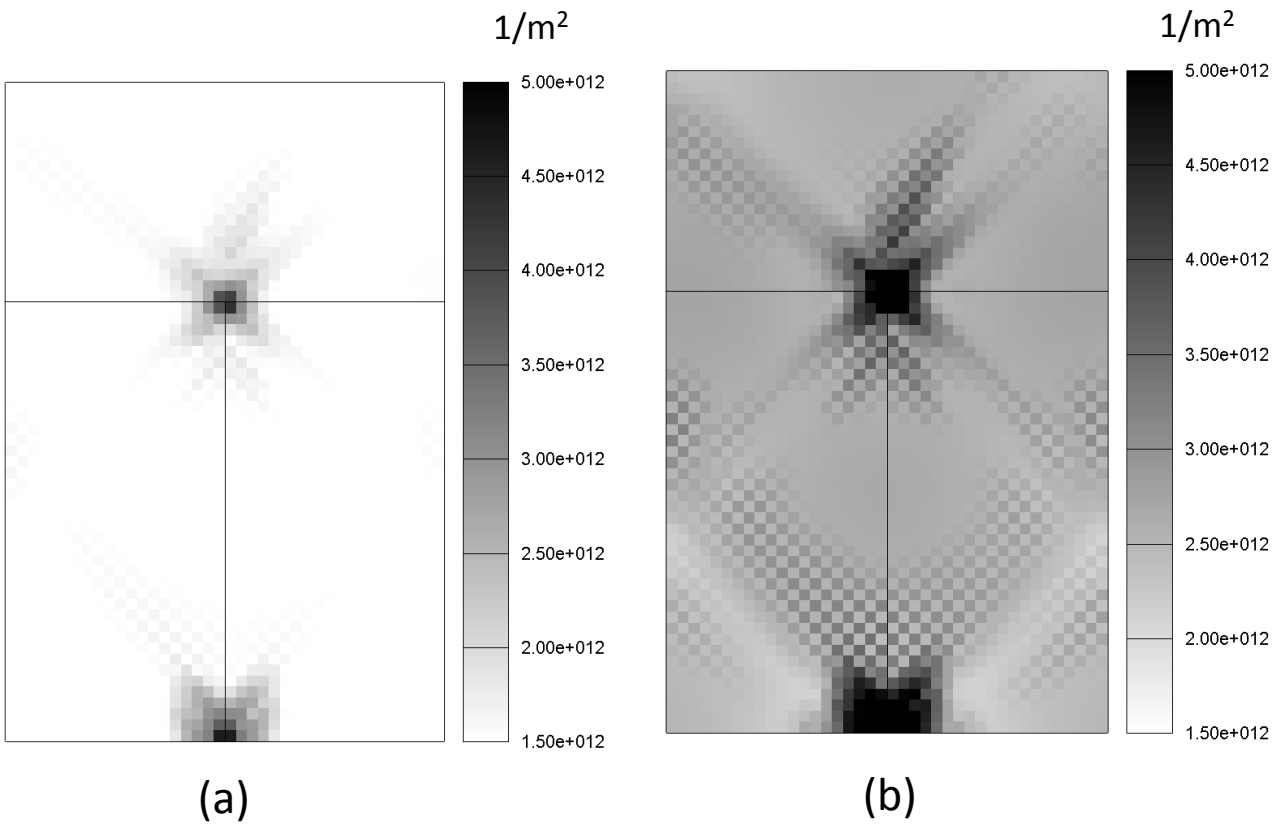

Fig. 14 Density distributions of the statistically stored dislocations on the B4 slip system and at the deformation stages **C** (a), and **E** (b).

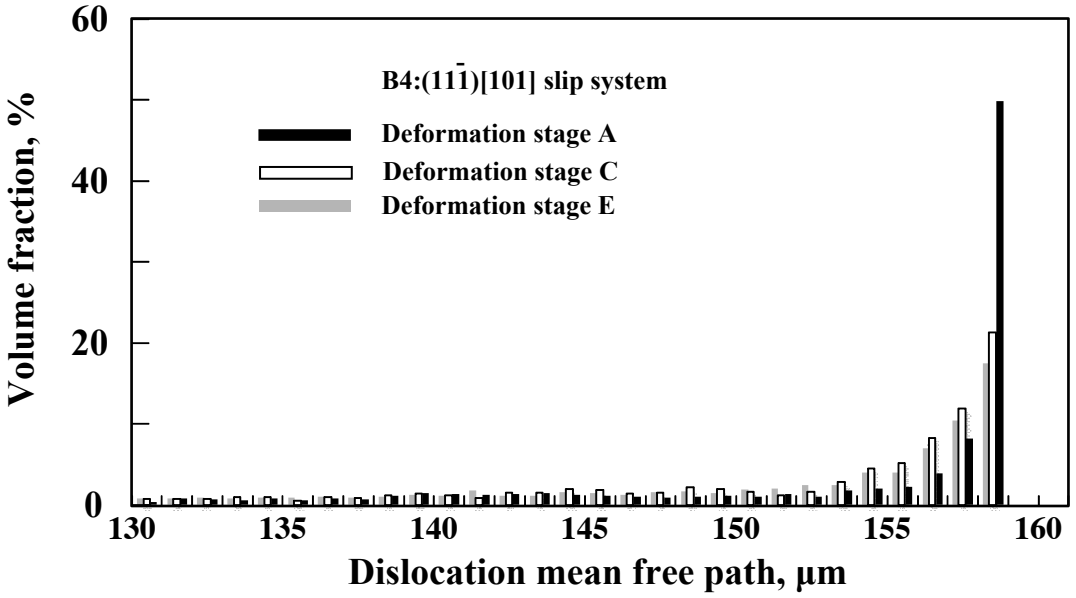

(a)

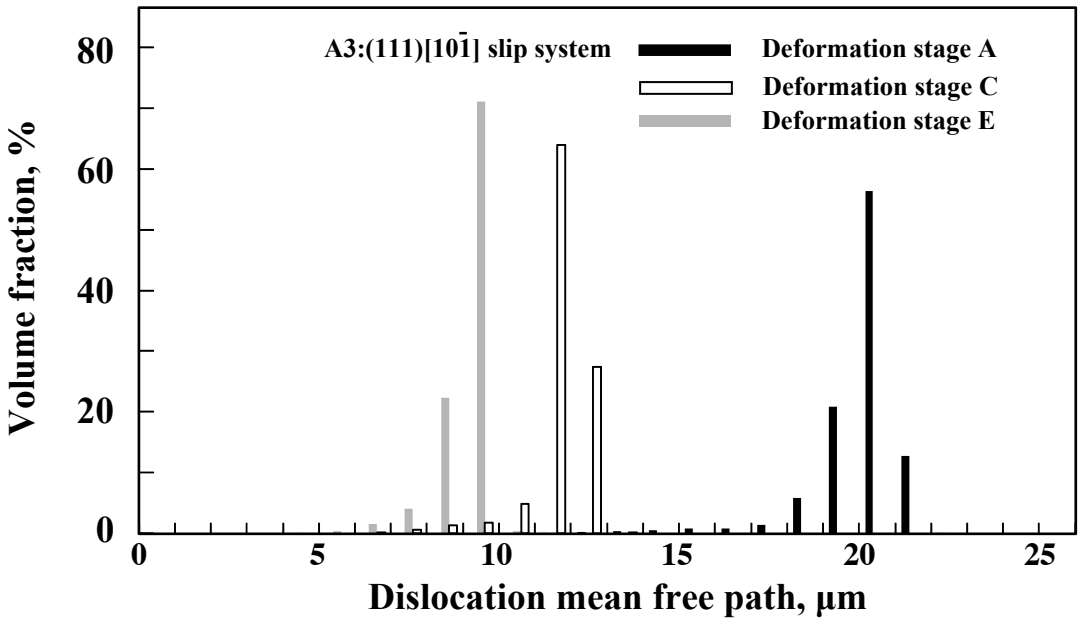

(b)

Fig. 15 Histograms of the dislocation mean free path for slip systems B4 (a), and A3 (b). At the deformation stage **A**, the mean free path on the B4 slip system is 158-159 μm in about 50 % volume of the tricrystal specimen. The mean free path on the A3 slip system and at deformation stages **A**, **C** and **E** are close to 20, 11 and 9 μm, respectively, in the entire region of the specimen, while slip on this system takes in a small fraction of the volume.

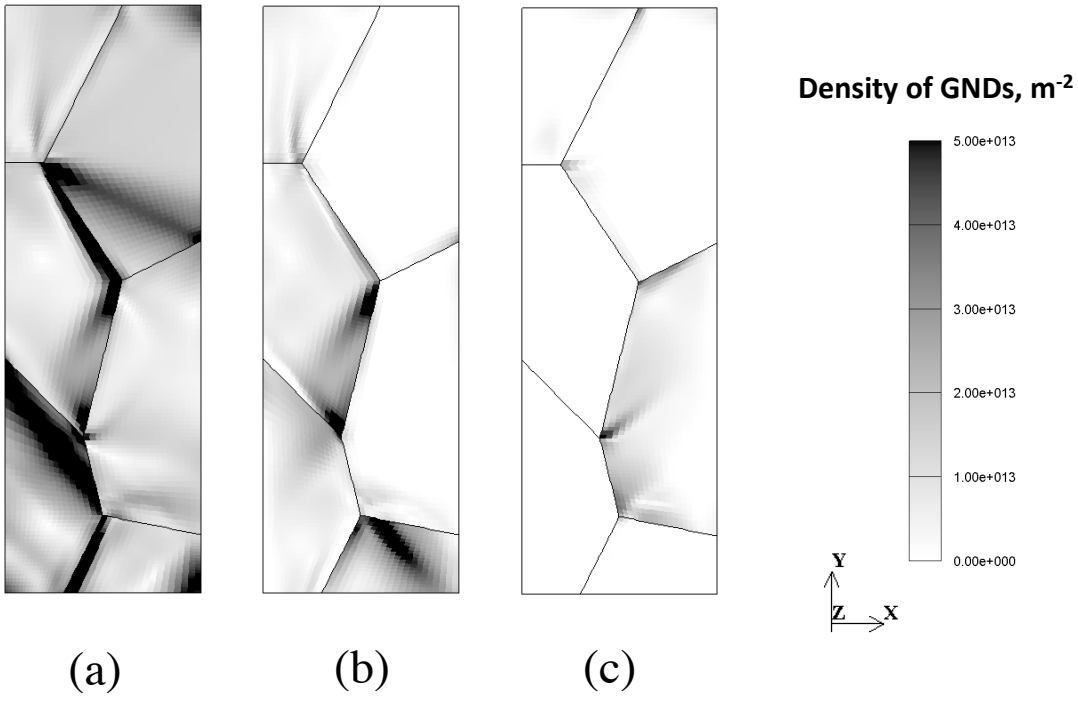

Fig. 16 Distribution of the density norm of GNDs on (a)B4, (b)A3, and (c)C1 slip systems in a six-grained multicrystal specimen [28,33]. Dimension of the specimen is 5x15x1 μm. The specimen was monotonically tensile deformed in *y*-direction and the nominal strain was 1%.